

# I/O-efficient iterative matrix inversion with photonic integrated circuits

Minjia Chen<sup>1</sup>, Yizhi Wang<sup>1</sup>, Chunhui Yao<sup>1</sup>, Adrian Wonfor<sup>1</sup>, Shuai Yang<sup>1</sup>, Richard Penty<sup>1</sup>, Qixiang Cheng<sup>1\*</sup>

1. Centre for Photonic Systems, Electrical Engineering Division, Department of Engineering, University of Cambridge, Cambridge, CB3 0FA, UK

*\*Corresponding author: qc223@cam.ac.uk*

## Abstract

Photonic integrated circuits have been explored extensively for optical processors with the aim of breaking the speed bottleneck of digital electronics in special-purpose tasks. Here we report a novel photonic iterative processor (PIP) for matrix inversion that underpins a wide range of scientific and engineering problems. A direct reuse of inputted data in the optical domain unlocks the potential to break the input/output bottleneck, which is regarded as one of the key barriers for optics to gain real benefits over electronics for computing. We demonstrate a lossless PIP for real-valued matrix inversion and use it to solve integral and differential equations. We further demonstrate a coherent PIP with optical loops integrated on-chip, enabling complex-valued computation and a net inversion time of 900ps. With much less demand for data movement among compute and memory units, at least an order of magnitude computation speed enhancement by using such a PIP over a single-pass optical processor is estimated for ridge regression task in both house price prediction and MNIST training.

## Introduction

Large scale computation is fundamental to modern life, underpinning massive applications ranging from cloud computing for basic computing needs, intelligent computing for artificial intelligence to supercomputing for scientific modelling and simulation<sup>1,2</sup>. Speed and power efficiency have become two key limitations of traditional von Neumann digital electronic computers as computing power demand has increased explosively during the past few years<sup>3-6</sup>. Over the past decades, extensive efforts have been made under the electronic computing paradigms. This includes next generation transistors made from novel materials<sup>7-9</sup>, heterogeneous processing units<sup>10</sup> that enable the synergy of central processing units (CPUs) and other paralleled accelerators, non-von Neumann architectures such as in-memory computing<sup>11-13</sup> and neuromorphic computing<sup>14,15</sup> that are suitable for fast and energy-efficient analogue computing, and advanced electronic-photonic co-packaging schemes that enhance the inter-chip or intra-chip communication bandwidths<sup>16</sup>.

Beyond the electronic computing regime, recent years have seen a surge in research into analogue photonic computing, which has long been considered as a promising alternative because of its ultra-fast in-propagation computation speed, inherent potential for high parallelism, large bandwidth and relatively low power consumption<sup>17-20</sup>. Integrated waveguide systems, which are built upon compact and phase-stable platforms, are becoming the mainstream for photonic computing innovations. Multiple degrees of freedom of light signals, including wavelength, polarization, space and mode, allow highly parallel information processing. Integrated meta-structures have been demonstrated for compact, ultra-fast, low-power and parallel computation, with applications in image differentiation<sup>21</sup> and solving integral equations<sup>22,23</sup>. The reconfigurable photonic circuits with Mach-Zehnder interferometers (MZIs) or tunable weight units for signal processing<sup>24-30</sup> and computing<sup>31-36</sup> receive the most attention.

Reported photonic integrated processors so far essentially perform matrix-vector multiplications in a single-pass manner<sup>19</sup>. Challenges can still arise from the optics and electronics interfaces, i.e., input/output bottlenecks in speed and power consumption. A single-pass optical matrix-vector multiplier implements  $O(N^2)$  operations with an IO cost of  $O(N)$ , corresponding to a computation-to-IO (C-to-IO) ratio<sup>37</sup> of  $O(N)$ . To keep pace with the ever-growing amount of data, the C-to-IO ratio needs to be largely enhanced to unlock a greater power of optical

processors. Being capable of processing signals recursively in the optical domain, photonic iterative processors (PIPs) can in turn reduce the IO demand in tasks, and hence significantly improve the C-to-IO ratio. We show that such PIPs can effectively and efficiently handle matrix inversions, a computationally expensive but fundamental task to a set of scientific and engineering problems. For applications such as solving linear systems in the analysis of physical or engineer models, ridge regression in statistical analyses, and more complex algorithms in machine learning tasks, the involved large sparse matrix inversions are generally solved by iterative algorithms for high efficiency<sup>38</sup>. For an iterative processor that implements a task in  $P$  iterations, the C-to-IO ratio reaches  $O(P \cdot N)$ . In the case of using a PIP for matrix inversion in a ridge regression task,  $P = O(N^{0.42})$  (Supplementary 1.3). This corresponds to a C-to-IO ratio of  $O(N^{1.42})$ , which indicates that the PIP can bring about an I/O efficiency breakthrough in dealing with tasks where iterative inversions are involved.

In this paper, we report a novel PIP based on reconfigurable photonic integrated circuits that goes beyond linear matrix multiplication and addition. The optical loopback enables iterative computations for direct matrix inverting with an enhanced I/O efficiency. The processor core is a matrix-vector multiplier comprising MZI units. Computation overhead is reduced by encoding the matrix elements directly on MZI arrays. The option of including optical switches in this device offers the flexibility of terminating the iterative process that eases the calibration and restoration processes. We demonstrate, to the best of our knowledge, the first lossless reconfigurable PIP system that is capable of directly inverting matrices and solving integral and differential equations. Such a PIP system computes  $4 \times 4$  real-valued matrix inversions with an accuracy of  $>97\%$ , and a net inversion time of 650 ns, which is solely bounded by the length of fibre-based optical loops. The lossless PIP is then reconfigured to numerically solve real-valued integral and differential equations, reaching a mean absolute error of  $< 0.02$ . The first coherent PIP with on-chip optical loops is also demonstrated to break the loop-length limitation on the net inversion time. The coherent PIP is demonstrated to operate  $2 \times 2$  complex-valued matrix inversions with an accuracy of  $> 98\%$ , and a net inversion time of 900 ps. Benefiting from the much-reduced IO demand, the proposed PIP is capable of reaching over an order of magnitude processing time enhancement compared with a single-pass optical processor, by emulating ridge regression tasks in house price prediction and training of MNIST dataset. Our results indicate a promising way towards ever-powerful optical processors that could surpass IO limits.

## Results

### Photonic iterative processor architecture

The proposed PIP is tailored for matrix inversion problems that cannot be easily solved by traditional single-pass photonic processors. Solving integral and differential equations can be reduced to basic matrix computations including addition, subtraction, multiplication and inversion, which can all be solved optically by iterative algorithms using the PIP. Matrix inversion is computed through the Richardson method:

$$\mathbf{X}^{(k+1)} = (\mathbf{I}_N - \omega \mathbf{A})\mathbf{X}^{(k)} + \omega \mathbf{I}_N \quad (k = 0, 1, 2, \dots) \quad (1)$$

where  $\mathbf{A}$  is an  $N \times N$  matrix operand to be inverted,  $\mathbf{I}_N$  is the  $N \times N$  identity matrix,  $\omega$  is a parameter used to adjust the convergence of the inversion algorithm and the matrix operand is encoded in the weight bank via  $\mathbf{I}_N - \omega \mathbf{A}$ .  $\mathbf{X}^{(k+1)}$  and  $\mathbf{X}^{(k)}$  are output matrices after  $k+1$  and  $k$  iterations, and  $\mathbf{X}^{(0)} = \omega \mathbf{I}_N$  is the initial input matrix that initiates the computation. The PIP generates matrix computation results one column at a time. Full-matrix inversion can be realised by using  $N$  PIPs or by a multiplexing technique based on a different architecture we proposed<sup>39</sup>.

Fig. 1 depicts the architecture of the proposed PIP based on Richardson method, with grey arrows indicating signal flows. As highlighted by red arrows, the input pulse (representing the  $j^{\text{th}}$  column of the initial input matrix,  $\omega \mathbf{e}_j$ ) is generated by modulating continuous wave (CW) lasers in modulators. Upon entering the loop, part of the pulse is split and sent to detectors for outputs readout (one column of  $\mathbf{X}^{(k+1)}$ ). The remaining part first passes an  $N \times N$  weight bank with each MZI encoding one element of the  $N \times N$  matrix,  $\mathbf{I}_N - \omega \mathbf{A}$ . Subsequently, the

weighted pulses are summed by waveguide couplers to implement matrix-vector multiplication (MVM). The MVM results (one column of  $(\mathbf{I}_N - \omega\mathbf{A})\mathbf{X}^{(k)}$ ) are then amplified to compensate for any loop loss. Optical filters are attached to remove excess amplified spontaneous emission (ASE) noise. The “clean” pulses now complete operations in one iteration and are either dropped or retained for recursive computing depending on the configuration of the optical switches. When the switches are “On”, the “clean” pulses are sent for summation with the input pulse (between one column of  $(\mathbf{I}_N - \omega\mathbf{A})\mathbf{X}^{(k)}$  and one column of  $\omega\mathbf{I}_N$ ). Then part of the summed signals is split out and detected for outputs. The remaining parts enter the next circulation for iterative computation. Such recursive operation is terminated either when the optical switches are set to “Off” or when the input pulse ends.

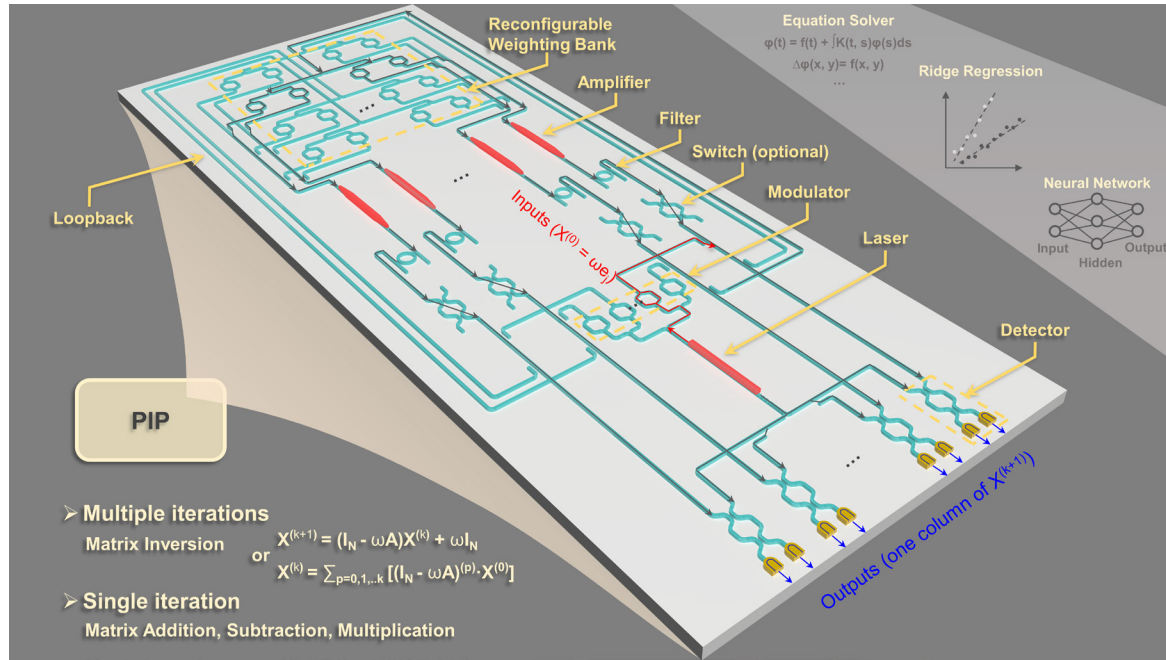


**Figure 1 | Conceptual figure of the photonic iterative processor (PIP).** Architecture of the proposed iterative photonic processor. The PIP serves as a photonic accelerator for inverting matrices which is widely used in equation solving, communication systems, robotics trajectory control, etc. Matrix inversion is solved by the Richardson method, whose results can be obtained by multiple iterations of the light signal in the PIP. Matrix addition, subtraction, and multiplication results can also be computed by a single iteration of the light signal in the PIP.

Alternatively, a direct expression of  $\mathbf{X}^{(k)}$  can be derived using the recursive expression shown in Eq. (1):

$$\mathbf{X}^{(k)} = \sum_{p=0}^k [(\mathbf{I}_N - \omega\mathbf{A})^{(p)} \cdot \mathbf{X}^{(0)}] \quad (\mathbf{X}^{(0)} = \omega\mathbf{I}_N, k = 0, 1, 2, \dots). \quad (2)$$

Eq. (2) indicates another approach to compute the inverse matrix using a short input pulse. An input pulse with a duration shorter than the light propagation time in a full loop can be used to encode one column of  $\mathbf{X}^{(0)}$ . In each iteration, the PIP effectively outputs  $(\mathbf{I}_N - \omega\mathbf{A})^{(p)} \cdot \mathbf{X}^{(0)}$ . The summation is then post-processed to generate final results. The PIP is also capable of computing matrix addition and multiplication in a single iteration by proper configuration. Detailed descriptions can be found in the supplementary 5.2.

## Real-valued matrix inversions

A 4×4 chip is taped out on the Silicon Nitride (SiN) platform, which is used as a processor core to form a lossless PIP system with off-the-shelf components as shown in Fig. 2a. The SiN chip integrates 4 adders, 4 splitters with a 4×4 sized MZI weighting bank, and their enlarged views are shown in Fig. 2b-d, respectively. Light is coupled in and out of the chip via edge couplers. Complete optical loopback paths are formulated by fibre components. The continuous-wave (CW) laser and optical modulator (Mod) correspond to the laser and modulator

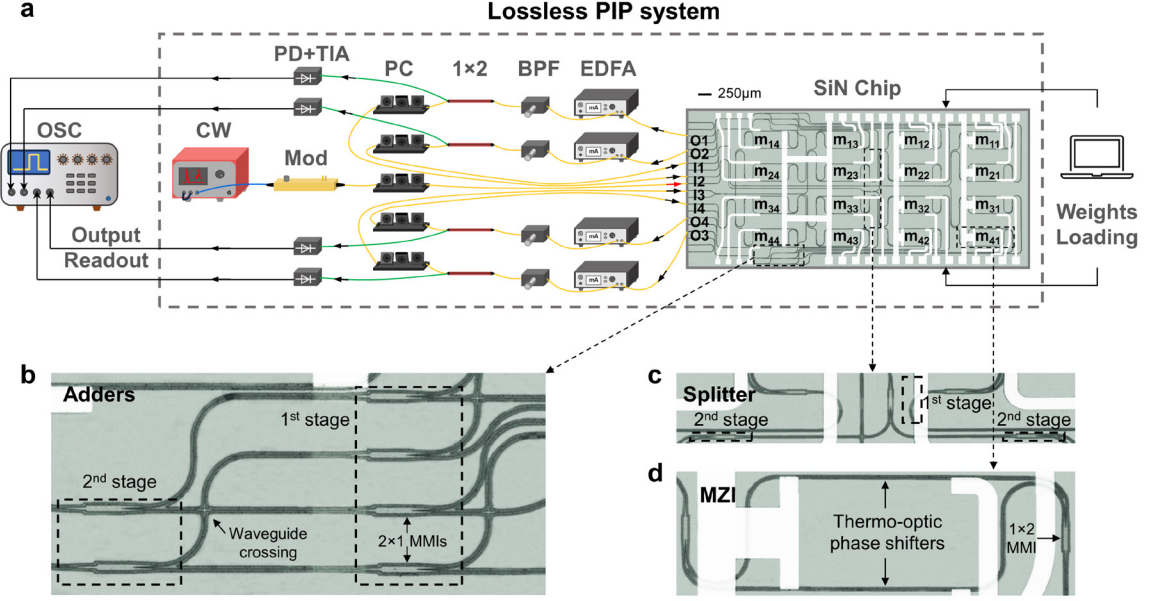


**Figure 2 | Lossless PIP system with a SiN chip core.** (a) Experimental set-up of the lossless PIP system. (b) Enlarged view of two adders comprising two stages of cascaded  $2 \times 1$  multimode interferometers (MMIs). (c) Enlarged view of a splitter consisting of two stages of cascaded  $1 \times 2$  MMIs. (d) Enlarged view of a weight unit comprising of a  $1 \times 1$  thermo-optic (TO) MZI.

blocks in Fig. 1, generating an input vector  $\omega e_j$  that is coupled into the  $4 \times 4$  chip. One column of the inverse results is computed each time by launching an optical input pulse to one input port and full matrix inversion is realized by sweeping different input ports (I1 – I4). The input pulse is first split into four copies on chip and then

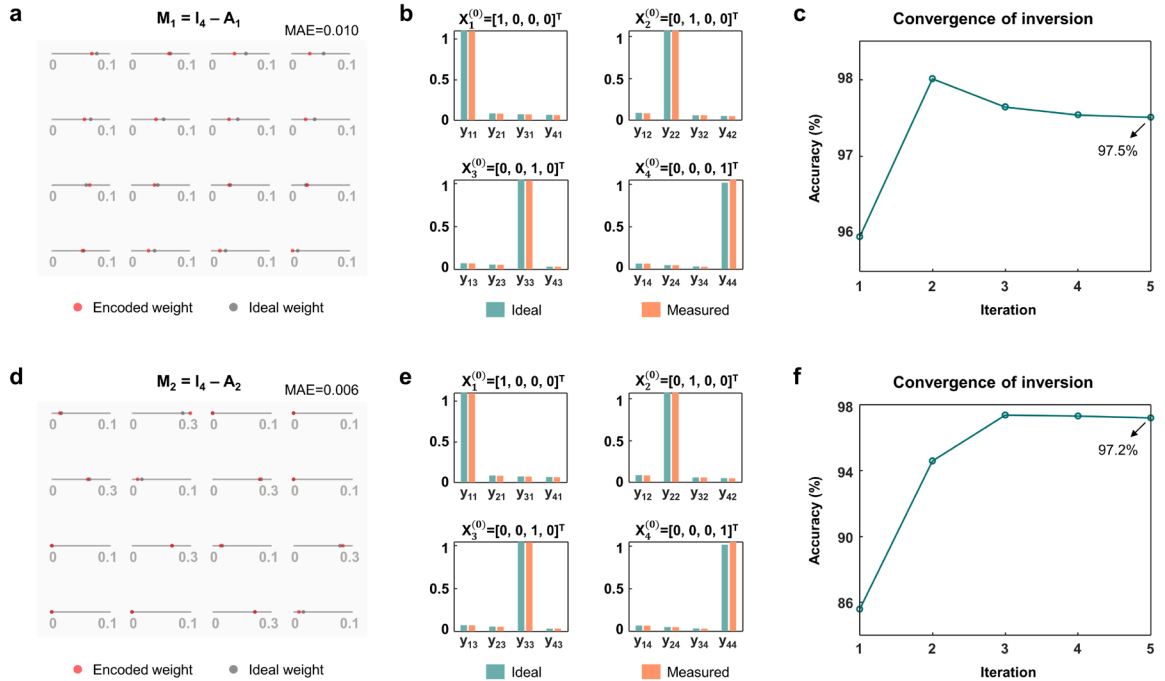


**Figure 3 | Real-valued matrix inversion examples.** (a) Ideal and encoded weight matrix  $M_1$ . MAE: Mean absolute error.  $MAE = \frac{1}{16} \sum_{j=1}^4 \sum_{i=1}^4 |M^{encode}(i, j) - M^{ideal}(i, j)|$ . (b) Ideal and measured inverse matrix  $A_1^{-1}$ .  $X_j^{(0)}$  is the  $j^{th}$  column of the initial input matrix  $X^{(0)}$ . (c) Evolution of inversion accuracy of  $A_1$  during convergence. Accuracy =  $(1 - \|A_{meas}^{-1} - A_{ideal}^{-1}\| / \|A_{ideal}^{-1}\|) \times 100\%$ . (d) Ideal and encoded weight matrix  $M_2$ . (e) Ideal and measured inverse matrix  $A_2^{-1}$ . (f) Evolution of inversion accuracy of  $A_2$  during convergence.

gets imprinted by the set of weights. The weighted signals are subsequently summed by 4 adders to perform an MVM, which are then coupled out of the chip and amplified by Erbium-doped fibre amplifiers (EDFAs), followed by bandpass filters (BPFs) to suppress ASE noises. The 1×2 splitters allow part of the optical signals to be collected by the oscilloscope (OSC) after outputs readout in photodetectors (PDs) and transimpedance amplifiers (TIAs), while the remaining part are sent back to the chip via the optical loops. Polarisation controllers (PCs) are used to align the polarisation state of optical inputs to the chip. Electrical control is used for loading matrix weights, setting the modulator and operating outputs readout.

We use the set-up shown in Fig. 2a to demonstrate two real-valued matrix inversion examples. The matrices to be inverted are:  $\mathbf{A}_1 = [0.92, -0.07, -0.06, -0.06; -0.07, 0.94, -0.05, -0.04; -0.06, -0.05, 0.97, -0.02; -0.06, -0.04, -0.02, 0.99]$  and  $\mathbf{A}_2 = [0.98, -0.26, 0, 0; -0.19, 0.98, -0.25, 0; 0, -0.2, 0.98, -0.24; 0, 0, -0.21, 0.98]$ . As shown in Fig. 3a and Fig. 3d,  $\mathbf{A}_1$  and  $\mathbf{A}_2$  are loaded into the weighting bank as  $\mathbf{M}_1 = \mathbf{I}_4 - \mathbf{A}_1$  and  $\mathbf{M}_2 = \mathbf{I}_4 - \mathbf{A}_2$  respectively (See Methods and Supplementary for matrix weights calibration). By injecting different unit vectors  $\mathbf{x}_j^{(0)} = \mathbf{e}_j$  ( $j = 1, 2, 3, 4$ ), different columns of the inversed matrices are obtained. Fig. 3b and Fig. 3e indicate a very good agreement between the ideal inverse results and the measured inverse results for the two inversion examples, respectively. The evolutions of inversion accuracy of  $\mathbf{A}_1$  and  $\mathbf{A}_2$  during convergence are traced and exhibited in Fig. 3c and Fig. 3f, reaching an inversion accuracy of 97.5% and 97.2% respectively.

## Real-valued integral and differential equation solving

Integral and differential equations offer a powerful tool for quantifying the dynamics of systems that change over time or space, making them widely used in scientific research and engineering. Analytical solutions can be accurate but are only available to simple and well-defined problems<sup>38</sup>. Numerical solutions are thus usually taken

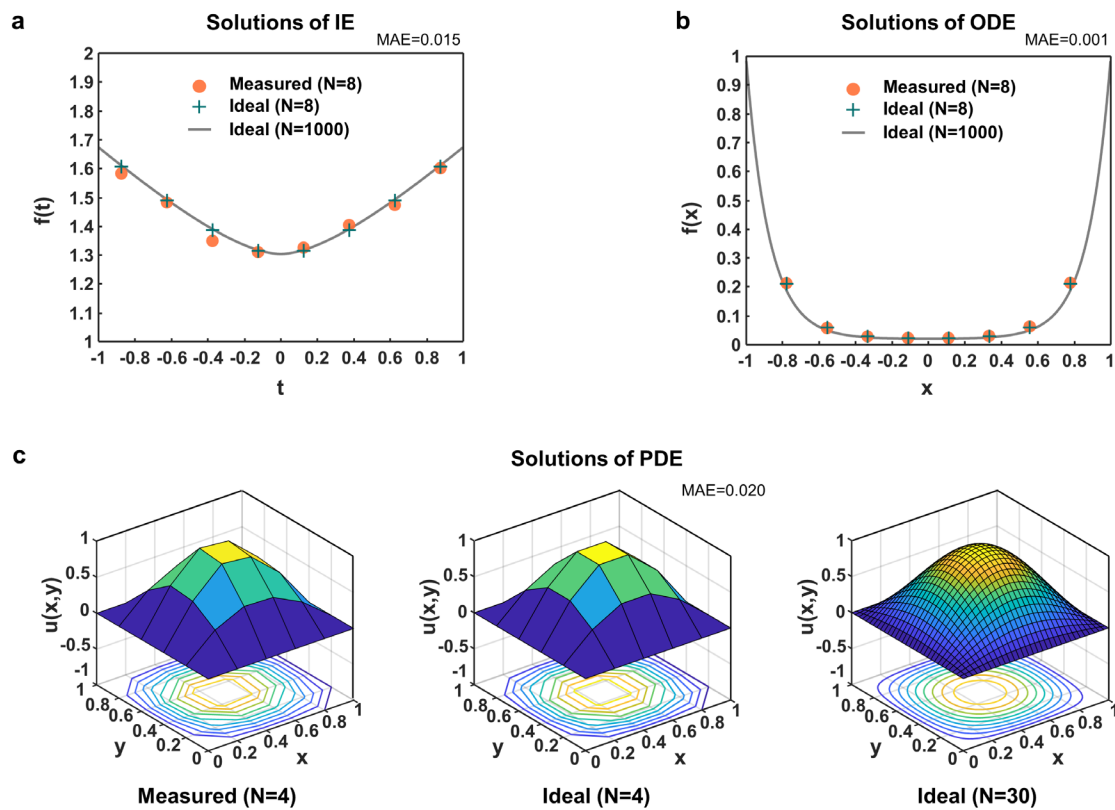


**Figure 4 | Solving real-valued integral and differential equations.** (a) Solutions to a Fredholm integral equation of the second kind. (b) Solutions to the 2<sup>nd</sup> order ordinary differential equation. (c) Solutions to the partial differential equation (Poisson equation). Mean absolute errors (MAEs) are indicated at the top of each sub figure.

for complex and real-world problems, albeit the fact that iterative algorithms are needed with necessary and frequent movement of very large amounts of data among the compute and memory resources, even with single-pass optical accelerators. Such data movement also dominates energy consumption<sup>12</sup>. The lossless PIP system that operates iteratively, however, is capable to directly solve integral and differential equations, providing a novel computing paradigm that significantly reduces the demand of data movement. We adopt the system to solve an integral equation (IE, Fredholm integral equation of the second kind, Eq. (3a)), a second order ordinary differential equation (2<sup>nd</sup> order ODE, Eq. (3b)) with both using an 8-point discretization, and a partial differential equation (PDE, Poisson equation, Eq. (3c)) using a 4-point discretization.

$$f(t) = 1 + \int_{-1}^1 0.2\sqrt{t^2 + s^2}f(s)ds, t \in [-1,1] \quad (3a)$$

$$d^2/dx^2 [f(x)] - 2x \cdot d/dx [f(x)] - 50f(x) = -1, x \in [-1,1], f(-1) = f(1) = 1 \quad (3b)$$

$$\partial^2 u(x,y)/\partial x^2 + \partial^2 u(x,y)/\partial y^2 = -2\pi^2 \sin(\pi x) \sin(\pi y), x, y \in [0,1], \partial_u = 0 \quad (3c)$$

An  $N$ -point discretization corresponds to  $N \times N$  matrix computations for IE and ODE, while it corresponds to  $N^2 \times N^2$  matrix computations for PDE. Block matrix computation techniques are employed to bridge the size of the problem and our chip, which could be readily mitigated by integrating a larger-scale processor on chip. Figure 4a-c showcase the measured solutions based on the chosen discretization resolution, ideal solutions (from a conventional 64-bit digital computer) based on the chosen discretization resolution, and ideal solutions based on a finer discretization resolution, respectively. Mean absolute errors (MAEs =  $\frac{1}{n} \sum_{j=1}^n |x_j^M - x_j^I|$ ,  $x^M$  is the measured solution,  $x^I$  is the ideal solution using the same discretization resolution) are shown at the top of each sub figure, indicating a very good agreement between the measured solutions and ideal solutions.

## Complex-valued matrix inversions

Currently, most photonic processors focus on real-valued computations, while complex-valued computations

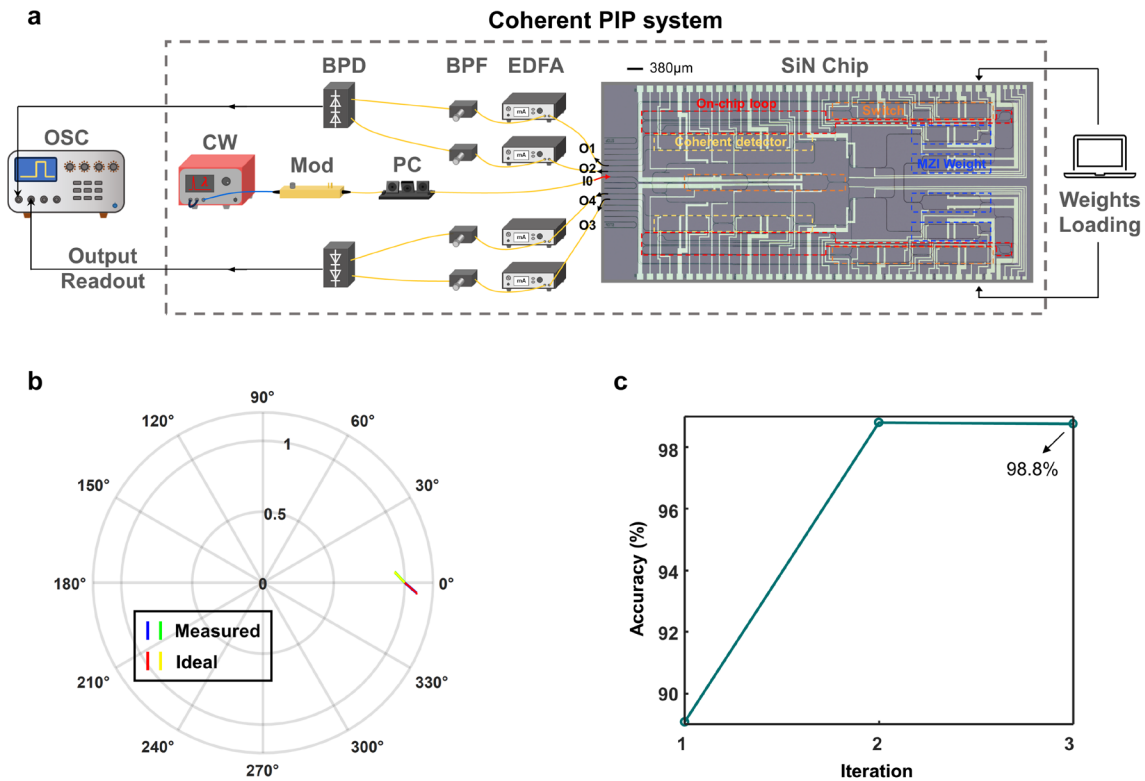


**Figure 5 | Demonstrated coherent PIP system and complex-valued matrix inversions.** (a) Experimental set-up of the coherent PIP system. (b) Ideal and measured inversion process of two diagonal elements of  $A_3$ . (c) Evolution of inversion accuracy of  $A_3$  during convergence.



may outperform their real-valued counterparts given the higher representational capacity<sup>36</sup>, especially in wireless communication systems<sup>40</sup>. By manipulating amplitude and phase of optical signals simultaneously, photonic processors are capable of performing truly complex-valued computations. This significantly enhances the processing efficiency compared with traditional electronic processors which store a complex number as two real parts and process each part separately.

Here we show a coherent PIP system as shown in Fig. 5a for complex-valued matrix inversions. With optical loopback paths integrated on-chip, stable phase control can be achieved together with ultrafast processing time. Optical switches are integrated on-chip to facilitate device calibration. Coherent outcomes are read out by off-chip balanced photodetectors (BPD) and captured in the OSC. EDFAs are used to compensate for coupling loss only and BPFs are used to remove excess ASE noise. The coherent PIP system is used to find the inverse of  $\mathbf{A}_3 = [0.92 + 0.07i, 0; 0, 1.07 - 0.07i]$ . The measured inversion process is outlined in Fig. 5b, indicating a very good agreement with the ideal process. Figure 5c shows the evolution of inversion accuracy of  $\mathbf{A}_3$ , which converges to 98.8% after 3 iterations.

## Discussion

Both the lossless and coherent PIP systems are formed with a SiN chip core and off-the-shelf components. To improve the scalability, energy efficiency and cost-effectiveness of the PIP system, it is essential to move towards a fully integrated processor on a single chip, illustrated in Fig. 1. A number of hybrid and heterogeneous integration methods have been investigated to combine the power of III-V with the full capability of SOI, spanning from flip-chip bonding<sup>41</sup>, die/wafer bonding<sup>42,43</sup>, micro-transfer printing<sup>44</sup>, to direct epitaxial growth<sup>45,46</sup>. Epitaxial growth may represent an ultimate path but die/wafer bonding features a higher technology readiness level in a short term. Membrane technology<sup>47,48</sup>, such as the InP membrane on silicon (IMOS), also represents a significant platform

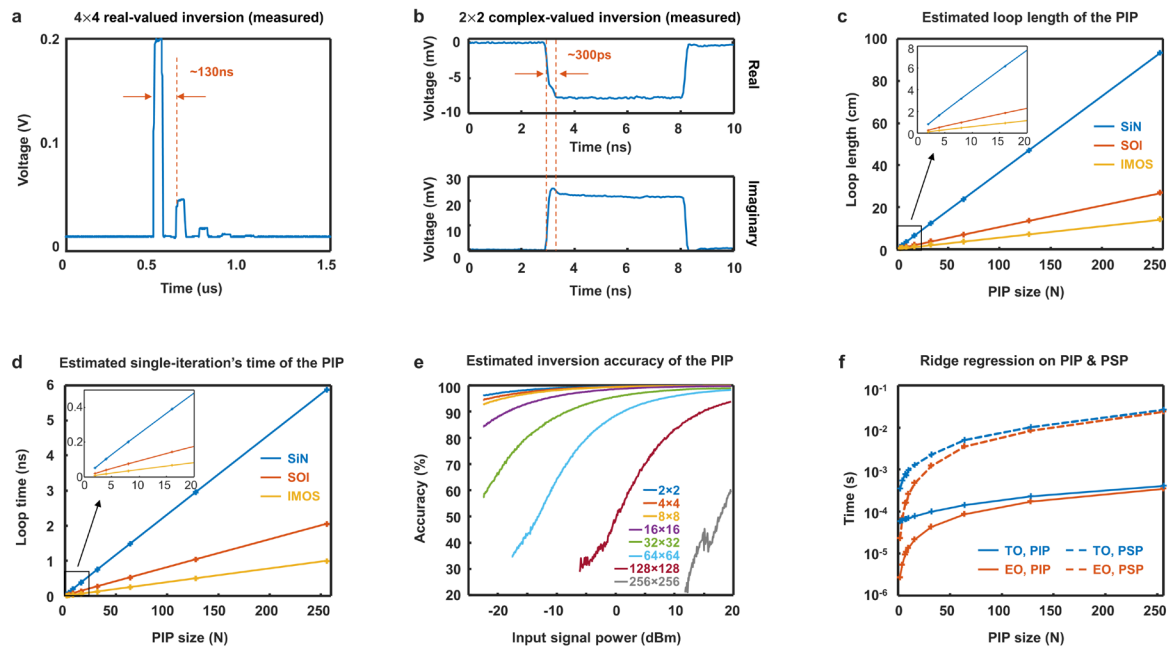


**Figure 6 | Further explorations on the processing time and scalability of the PIP.** Measured output waveforms of one element of (a) a 4×4 real-valued and (b) a 2×2 complex-valued inversion. (c) Estimated loop length of the fully integrated PIP with a size of 2×2 to 256×256 on three different integration platforms. (d) Estimated single-iteration's processing time of the fully integrated PIP with a size of 2×2 to 256×256 on three different integration platforms. (e) Estimated inversion accuracies of the PIP with a size of 2×2 to 256×256. (f) Comparison of the total time required for inversion in ridge regression task implemented in a PIP and a single-pass photonic processor. TO: thermo-optic tuning, EO: electro-optic tuning. PIP: photonic iterative processor, PSP: photonic single-pass processor.

that co-integrates passive and active components. Also, high bandwidth modulators and photodetectors are available on the silicon-on-insulator platform<sup>49</sup>, III-V platform<sup>50,51</sup> and the hybrid integration platform<sup>52,53</sup>. The capability of reconfiguring phase shifters can at nanosecond- or even picosecond-scales can significantly reduce the weights reloading time, achieving even faster computations.

The net inversion time of a PIP system is determined by the pulse propagation time within one loop together with the number of iterations to reach convergence. Figure. 6a and 6b presents the time-traced output waveforms of one element in the 4×4 real-valued and 2×2 complex-valued inversion, respectively. Their corresponded pulse propagation time of one iteration is 130 ns and 300 ps, respectively, which is solely determined by the optical loop length. It's worth noting that for the coherent PIP device, additional delay lines (~3.9 cm) are integrated as part of the loopback paths to ease the electrical readout, which can be shorted for a faster computation speed. The number of iterations required for convergence for the Richardson method is at least (See Supplementary 1.2):

$$P = \frac{\ln(1/\epsilon)}{\ln|[(\lambda_N + \lambda_1)/(\lambda_N - \lambda_1)]|} \quad (4)$$

making the net inversion time of 650 ns and 900 ps for the 4×4 and 2×2 cases, respectively (measurement shown in Fig. 6a). Figure 6c estimates the loop length of a monolithic PIP with a size of 2×2 to 256×256 on three different material integration platforms (See Supplementary 6.1 for detailed loop length estimations). Their corresponding processing time in a single iteration is shown in Fig. 6d. The estimated inversion accuracies considering the ASE noise, encoding noise, and detection noise are shown in Fig. 6e. These results indicate a good scalability of the PIP.

Finally, we compare the processing time of the ridge regression task, which forms the cornerstone in a set of statistical analyses and machine learning algorithms, implemented on a PIP and on a single-pass processor. The ridge regression task writes as:  $\hat{\beta} = (X^T X + \lambda I)^{-1} X^T y$ , where  $\hat{\beta}$  is the parameter vector to be fitted (solved),  $X, y$ , respectively, are the independent and dependent variables that encode the samples,  $I$  is an identity matrix and  $\lambda$  is a constant which is often varied to find the optimum fit. The inversion of  $X^T X$  undoubtedly dominates the processing time. Figure 6f shows a comparison of the total time required for one ridge regression task implemented in a PIP and a single-pass photonic processor (See Supplementary 6.2 for details), indicating significant processing speed improvement of the PIP. We then apply the ridge regression in predicting house price to show the improvement in processing time owing to the enhanced IO efficiency. Using a house price dataset with seven parameters<sup>54</sup>, the processing time difference of a PIP and a single-pass processor for each  $\lambda$  is estimated to be 705  $\mu$ s and 150.6  $\mu$ s for TO and EO modulation, respectively (According to Fig. 6f, when processor size is 7, the processing time for each case is: TO on a PIP: 65  $\mu$ s; TO on a PSP: 770  $\mu$ s; EO on a PIP: 9.4  $\mu$ s; EO on a PSP: 160  $\mu$ s). For a conservative estimation of time, at least 1000 different  $\lambda$  is used in this task to find the optimal fit (Supplementary 8), leading to a total time difference of 41.5 s and 8.7 s for TO and EO modulation, indicating at least an order of magnitude speed enhancement of the PIP.

We further perform evaluations based on a more complicated task, i.e., training a neural network, to showcase the power of the PIP. The MNIST hand-written digit classification is a commonly used benchmark in neural network models. With the aid of reservoir computing, the training of the MNIST dataset can be simplified to a ridge regression task. In the case of training 60000 MNIST samples using a 10×10 PIP, 6000 regression estimation is needed in each epoch of training. The time difference in training 60000 MNIST samples for at least 10 epochs (Supplementary 8) using a PIP and a single-pass processor is 53 s and 16 s for TO and EO modulation, respectively.

Additionally, multiplexing is a promising way to unleash the power of inherently high parallelism of optical computing. Multiplexing in either optical frequencies<sup>37</sup> or radio frequencies<sup>55</sup> can notably increase the number of information processed simultaneously.

## Conclusion

In this paper, we propose a PIP with reconfigurable photonic circuits that is capable of handling signals in the



optical domain recursively, achieving much higher computation-to-input/output ratio than traditional single-pass optical processors. This heralds a new photonic computing paradigm that significantly reduces the data shuttling cost. We showcase the first lossless PIP and the first coherent PIP with on-chip optical loops to demonstrate its power. High-fidelity optical computations including real-valued matrix inversions, real-valued integral and differential equation solving, and complex-valued matrix inversions are performed. By emulating the ridge regression tasks such as house price prediction and MNIST dataset training, the proposed PIP is shown to be capable of reaching over an order of magnitude processing speed enhancement compared with a single-pass optical processor, benefiting from the much-reduced IO demand. Our work paves the way towards the next generation photonic processor that significantly enhances IO efficiency and processing speed.

## Methods

**Chip fabrication.** The photonic chip with a footprint of  $2.8 \times 6.6 \text{ mm}^2$  is fabricated on a SiN platform provided by CORNERSTONE multi-project wafer run using the standard deep ultraviolet lithography with a feature size of 250 nm. The platform comprises a 3  $\mu\text{m}$  buried oxide layer, and a 2  $\mu\text{m}$  silicon dioxide top cladding, and a 300 nm thick LPCVD SiN layer, which provides propagation loss of  $<1 \text{ dB/cm}$ . Basic building blocks including the strip waveguide, the  $1 \times 2$  MMI coupler, the  $90^\circ$  bend, the waveguide crossing and the edge coupler are customized using a commercial Lumerical FDTD simulator. The waveguide crossing has an extinction ratio of  $>30 \text{ dB}$ . The edge coupler is based on a reverse taper structure, with a mode diameter of around 3.5  $\mu\text{m}$  and a coupling loss of  $\sim 2.5 \text{ dB}$  per facet.

**Chip characterization.** 16 MZI weights are calibrated independently by launching a laser into the chip and measuring the output light intensity while sweeping the applied voltage to the heaters on the MZI arms. 16 transmission-voltage (T-V) or transmission-power (T-P) curves are recorded and fitted to form lookup tables for loading matrix weights. The effective weight of each matrix element is a combination of the attenuation in the weighting bank, the loss in the loop including the MZI unit, and the gain in that loop. This is achieved by creating an optical loop between input and output waveguides for a single MZI. The effective weight is then determined by launching an optical pulse into the loop and measuring the ratio of subsequent output pulses. Note that there is an EDFA within the loop whose purpose is to compensate for optical losses in the loop. Finally the attenuation in the MZI unit is adjusted to provide the required attenuation for each matrix element.

**Experimental setup.** The light source (Thorlabs TLX1 tunable laser) is set to a 1550 nm wavelength and 5 dBm output power. Manual polarisation controllers are used to align light polarisations to the chip. The optical switch is Thorlabs LNA6213 intensity modulator. Amplifiers are EDFAs from Connect Laser which can provide  $>35 \text{ dB}$  gain. BPFs are filters from WL Photonics with 0.1 nm 3 dB bandwidth. Outputs are recorded in a 4-channel Keysight DSO-S 404A oscilloscope. The system requires electrical control. A customized Matlab program is used to characterize the chip. The switch is controlled by a Tektronix AFG3102C function generator. Outputs from the oscilloscope are sent back to an electronic computer for analysis.

**Numerical methods.** Discretization is needed for numerically solving equations (see Supplementary 2). The rectangular integration technique is used for solving integral equations by approximating the integral by summing a series of rectangular partitions under the curve. Fredholm integral equations of the second kind can be written as

$$f(t_i) = c(t_i) + \frac{b-a}{N} \cdot \sum_{j=1}^N K(t_i, s_j) f(s_j). \quad (6)$$

$[a, b] = [-1, 1]$  is the integral interval.  $N = 8$  is the number of equally divided subintervals of  $[a, b]$ . Assume the divisions are the same along both  $t$  and  $s$  axes.  $t_i$  and  $s_j$  ( $i, j = 1, 2, \dots, N$ ) are midpoints of the subintervals along both axes (called the discretized points).  $K(t_i, s_j)$  is the value of kernel function at the discretized point  $(t_i, s_j)$ .  $f(t_i)$  is the value of the function to be solved at discretized points  $t_i$ .  $c(t_i)$  is the value of the input function at

discretized points  $t_i$ . Eq. (2) can be expressed in a matrix form as  $\mathbf{f} = \mathbf{c} + \frac{b-a}{N} \mathbf{K} \mathbf{f}$ . The solution of the linear equation is  $\mathbf{f} = (\mathbf{I} - \frac{b-a}{N} \mathbf{K})^{-1} \mathbf{c}$ .

The finite difference method is used to solve differential equations by using finite difference formulas at evenly spaced grid points to approximate the differential equations. There are three types of difference formulas, which are central, forward and backward differences. Here we use central difference to approximate the equations. The first and second order derivatives of ODEs (1D system) can be written as

$$\frac{dy}{dx} = \frac{y_{i+1} - y_{i-1}}{2h} \quad (7)$$

$$\frac{d^2y}{dx^2} = \frac{y_{i+1} - 2y_i + y_{i-1}}{h^2} \quad (8)$$

where  $i$  is the index of the desired grid point,  $i-1$  and  $i+1$  are the indices of the neighbouring points, and  $h$  is the grid size. A fixed grid size is used for simplicity. For PDEs (2D system), the second order partial derivatives with respect to variable  $x$  and the gradient relationship can be written as

$$\frac{\partial^2 u(x,y)}{\partial x^2} = \frac{u_{i+1,j} - 2u_{i,j} + u_{i-1,j}}{h^2} \quad (9)$$

$$\Delta u(x,y) = \frac{\partial^2 u(x,y)}{\partial x^2} + \frac{\partial^2 u(x,y)}{\partial y^2} = \frac{u_{i+1,j} + u_{i,j+1} - 4u_{i,j} + u_{i-1,j} + u_{i,j-1}}{h^2} \quad (10)$$

The discretized equations (6)-(10) are then mapped into coefficient matrices which describes the relation between a point and other points in the grid. Solving differential equations are then converted to solving matrix inversions.

## Acknowledgement

This work was supported by the European Union's Horizon 2020 research and innovation programme, project INSPIRE, and UK EPSRC, project QUDOS (EP/T028475/1). The authors thank CORNERSTONE for providing free access to their second SiN MPW run (funded by the CORNERSTONE 2 project under Grant EP/T019697/1). The authors also thank Dr. Mark Holm and Mr. Zexing Li for helpful discussions.

## Author contributions

M.C. and Q.C. conceived the idea. M.C. performed numerical simulations, designed the schematics of the photonic chips, built the experimental set-ups, conducted the experiments with helpful advice from A.W., S.Y. and Q.C., and analysed the results. Y.W. helped with the coherent PIP test. and conducted simulations on convergence iterations of the Richardson method and PIP processing time in ridge regression and MNIST training. C.Y. and M.C. designed the layouts of the photonic chips. M.C. and Q.C. wrote the manuscript, with inputs from all authors. Q.C. and R.P. supervised the project.

## Data availability

Additional data related to this publication is available at <https://doi.org/10.17863/CAM.????..>

## Competing interests

The authors declare no competing interests.

## References

1. CAICT - WHITE PAPER. [http://www.caict.ac.cn/english/research/whitepapers/202211/t20221111\\_411290.html](http://www.caict.ac.cn/english/research/whitepapers/202211/t20221111_411290.html).
2. Independent Review of The Future of Compute: Final report and recommendations. *GOV.UK* <https://www.gov.uk/government/publications/future-of-compute-review/the-future-of-compute-report-of-the-review-of-independent-panel-of-experts>.
3. Sevilla, J. Compute Trends Across Three Eras of Machine Learning. *Epoch* <https://epochai.org/blog/compute-trends> (2022).
4. Waldrop, M. M. The chips are down for Moore's law. *Nature News* **530**, 144 (2016).
5. Theis, T. N. & Wong, H.-S. P. The End of Moore's Law: A New Beginning for Information Technology. *Computing in Science Engineering* **19**, 41–50 (2017).
6. Shalf, J. The future of computing beyond Moore's Law. *Phil. Trans. R. Soc. A* **378**, 20190061 (2020).
7. Loubet, N. *et al.* Stacked nanosheet gate-all-around transistor to enable scaling beyond FinFET. in *2017 Symposium on VLSI Technology* T230–T231 (2017).

8. De Volder, M. F. L. *et al.* Carbon Nanotubes: Present and Future Commercial Applications. *Science* **339**, 535–539 (2013).
9. Bader, S. D. & Parkin, S. S. P. Spintronics. *Annual Review of Condensed Matter Physics* **1**, 71–88 (2010).
10. oneAPI: A New Era of Heterogeneous Computing. *Intel*  
<https://www.intel.com/content/www/us/en/developer/tools/oneapi/overview.html>.
11. Le Gallo, M. *et al.* Mixed-precision in-memory computing. *Nat Electron* **1**, 246–253 (2018).
12. Zidan, M. A. *et al.* A general memristor-based partial differential equation solver. *Nat Electron* **1**, 411–420 (2018).
13. Yao, P. *et al.* Fully hardware-implemented memristor convolutional neural network. *Nature* **577**, 641–646 (2020).
14. Mead, C. Neuromorphic electronic systems. *Proceedings of the IEEE* **78**, 1629–1636 (1990).
15. Mead, C. How we created neuromorphic engineering. *Nat Electron* **3**, 434–435 (2020).
16. Cheng, Q. *et al.* Recent advances in optical technologies for data centers: a review. *Optica* **5**, 1354 (2018).
17. Caulfield, H. J. & Dolev, S. Why future supercomputing requires optics. *Nature Photon* **4**, 261–263 (2010).
18. Solli, D. R. & Jalali, B. Analog optical computing. *Nature Photon* **9**, 704–706 (2015).
19. Zhou, H. *et al.* Photonic matrix multiplication lights up photonic accelerator and beyond. *Light Sci Appl* **11**, 30 (2022).
20. Xu, X.-Y. & Jin, X.-M. Integrated Photonic Computing beyond the von Neumann Architecture. *ACS Photonics* (2023).
17. Goodman, J. W. *et al.* Fully parallel, high-speed incoherent optical method for performing discrete Fourier transforms. *Opt. Lett.*, **OL 2**, 1–3 (1978).
18. Athale, R. A. & Collins, W. C. Optical matrix–matrix multiplier based on outer product decomposition. *Appl. Opt.*, **AO 21**, 2089–2090 (1982).
19. Rajbenbach, H. *et al.* Optical implementation of an iterative algorithm for matrix inversion. *Appl. Opt.*, **AO 26**, 1024–1031 (1987).
20. Qian, C. *et al.* Performing optical logic operations by a diffractive neural network. *Light Sci Appl* **9**, 59 (2020).
21. Zhou, Y. *et al.* Flat optics for image differentiation. *Nat. Photonics* **14**, 316–323 (2020).
22. Mohammadi Estakhri, N. *et al.* Inverse-designed metastructures that solve equations. *Science* **363**, 1333–1338 (2019).
23. Camacho, M. *et al.* A single inverse-designed photonic structure that performs parallel computing. *Nat Commun* **12**, 1466 (2021).
24. Miller, D. A. B. Establishing Optimal Wave Communication Channels Automatically. *Journal of Lightwave Technology* **31**, 3987–3994 (2013).
25. Liu, W. *et al.* A fully reconfigurable photonic integrated signal processor. *Nature Photon* **10**, 190–195 (2016).
26. Ribeiro, A. *et al.* Demonstration of a  $4 \times 4$ -port universal linear circuit. *Optica*, **OPTICA 3**, 1348–1357 (2016).
27. Annoni, A. *et al.* Unscrambling light—automatically undoing strong mixing between modes. *Light Sci Appl* **6**, e17110–e17110 (2017).
28. Harris, N. C. *et al.* Linear programmable nanophotonic processors. *Optica*, **OPTICA 5**, 1623–1631 (2018).
29. Bogaerts, W. *et al.* Programmable photonic circuits. *Nature* **586**, 207–216 (2020).
30. Zhou, H. *et al.* Self-Configuring and Reconfigurable Silicon Photonic Signal Processor. *ACS Photonics* **7**, 792–799 (2020).
31. Yang, L. *et al.* On-chip CMOS-compatible optical signal processor. *Opt. Express*, **OE 20**, 13560–13565 (2012).
32. Wu, J. *et al.* Compact tunable silicon photonic differential-equation solver for general linear time-invariant systems. *Opt. Express*, **OE 22**, 26254–26264 (2014).
33. Shen, Y. *et al.* Deep learning with coherent nanophotonic circuits. *Nature Photon* **11**, 441–446 (2017).
34. Shastri, B. J. *et al.* Photonics for artificial intelligence and neuromorphic computing. *Nat. Photonics* **15**, 102–114 (2021).
35. Feldmann, J. *et al.* Parallel convolutional processing using an integrated photonic tensor core. *Nature* **589**, 52–58 (2021).
36. Zhang, H. *et al.* An optical neural chip for implementing complex-valued neural network. *Nat Commun* **12**, 457 (2021).
37. McMahon, P. L. The physics of optical computing. *Nat Rev Phys* **1**–18 (2023).
38. Golub, G. H. & Van Loan, C. F. *Matrix computations*. (The Johns Hopkins University Press, 2013).
39. Chen, M. *et al.* Iterative photonic processor for fast complex-valued matrix inversion. *Photon. Res.* **10**, 2488 (2022).
40. Albreem, M. A. *et al.* Overview of Precoding Techniques for Massive MIMO. *IEEE Access* **9**, 60764–60801 (2021).
41. Lin, S. *et al.* Efficient, tunable flip-chip-integrated III-V/Si hybrid external-cavity laser array. *Opt. Express*, **OE 24**, 21454–21462 (2016).
42. Roelkens, G. *et al.* III-V/Si photonics by die-to-wafer bonding. *Materials Today* **10**, 36–43 (2007).
43. Liang, D. *et al.* Low-Temperature, Strong SiO<sub>2</sub>-SiO<sub>2</sub> Covalent Wafer Bonding for III–V Compound Semiconductors-to-Silicon Photonic Integrated Circuits. *J. Electron. Mater.*, **37**, 1552–1559 (2008).
44. Zhang, J. *et al.* III-V-on-Si photonic integrated circuits realized using micro-transfer-printing. *APL Photonics* **4**, 110803 (2019).
45. Shi, Y. *et al.* Optical pumped InGaAs/GaAs nano-ridge laser epitaxially grown on a standard 300-mm Si wafer. *Optica*, **OPTICA 4**, 1468–1473 (2017).
46. Scherrer, M. *et al.* In-Plane Monolithic Integration of Scaled III-V Photonic Devices. *Applied Sciences* **11**, 1887 (2021).
47. Matsuo, S. *et al.* Directly modulated buried heterostructure DFB laser on SiO<sub>2</sub>/Si substrate fabricated by regrowth of InP using bonded active layer. *Opt. Express*, **OE 22**, 12139–12147 (2014).
48. Jiao, Y. *et al.* Indium Phosphide Membrane Nanophotonic Integrated Circuits on Silicon. *Phys. Status Solidi A* **217**, 1900606 (2020).
49. Giewont, K. *et al.* 300-mm Monolithic Silicon Photonics Foundry Technology. *IEEE JOURNAL OF SELECTED TOPICS IN QUANTUM ELECTRONICS* **25**, (2019).
50. Ogiso, Y. *et al.* 80-GHz Bandwidth and 1.5-V V $\pi$  InP-Based IQ Modulator. *Journal of Lightwave Technology* **38**, 249–255 (2020).
51. Beling, A. & Campbell, J. C. InP-Based High-Speed Photodetectors. *Journal of Lightwave Technology* **27**, 343–355 (2009).
52. Alloatti, L. *et al.* 100 GHz silicon–organic hybrid modulator. *Light Sci Appl* **3**, e173–e173 (2014).
53. Wang, Y. *et al.* Bound-States-in-Continuum Hybrid Integration of 2D Platinum Diselenide on Silicon Nitride for High-Speed Photodetectors. *ACS Photonics* **7**, 2643–2649 (2020).

54. <https://www.kaggle.com/datasets/quantbruce/real-estate-price-prediction/code?datasetId=88705&sortBy=voteCount>
55. Dong, B. *et al.* Higher-dimensional processing using a photonic tensor core with continuous-time data. *Nat. Photon.* 1–9 (2023)